Interatomic orbital magnetism: The case of 3*d* adatoms deposited on the Pt(111) surface

Sascha Brinker,[*] Manuel dos Santos Dias,[†] and Samir Lounis[‡]
Peter Grünberg Institut and Institute for Advanced Simulation, Forschungszentrum Jülich and JARA, 52425 Jülich, Germany

(Received 23 February 2018; revised manuscript received 21 August 2018; published 27 September 2018)

The orbital magnetic moment is still surprisingly not well understood, in contrast to the spin part. Its description in finite systems, such as isolated atoms and molecules, is not problematic, but it was only recently that a rigorous picture was provided for extended systems. Here we focus on an intermediate class of systems: magnetic adatoms placed on a nonmagnetic surface. We show that the essential quantity is the ground-state charge current density, in the presence of spin-orbit coupling, and set out its first-principles description. This is illustrated by studying the magnetism of the surface Pt electrons, induced by the presence of Cr, Mn, Fe, Co, and Ni adatoms. A physically appealing partition of the charge current is introduced. This reveals that there is an important interatomic contribution to the orbital moments of the Pt atoms, extending three times as far from each magnetic adatom as the induced spin and atomic orbital moments. We find that it is as sizable as the latter and attribute its origin to a spin-orbital susceptibility of the Pt surface, different from the one responsible for the formation of the atomic orbital moments.

DOI: 10.1103/PhysRevB.98.094428

I. INTRODUCTION

Magnetic impurities bridge real and reciprocal space, endowing their nonmagnetic host materials with new properties built from the scattering of the itinerant electrons. The itinerant electrons are best understood in reciprocal space, while many of the effects due to impurity scattering are best understood in real space. The oscillations of the electron density predicted by Friedel [1] are a classic embodiment of this paradigm, with the giant magnetic moments induced in Pd and Pt attesting to it [2–8]. Friedel oscillations lead to long-range Ruderman-Kittel-Kasuya-Yosida (RKKY) interactions [9,10]. These stabilize helical magnetic chains, which might host Majorana states on superconductors [11–14], and affect the Kondo screening cloud [15]. Other examples, such as the anomalous Hall effect [16–18], Dzyaloshinskii-Moriya interactions [19–21], and large magnetic anisotropy energies [7,22–25], highlight the importance of spin-orbit coupling (SOC) for the impurity-driven physics. The induced magnetism of the itinerant electrons plays an important role in all of this, but important aspects remain to be explored.

The interplay between spin and orbital degrees of freedom also underlies one of the most fundamental magnetic properties, the orbital moment [26–30]. It can be quantified through the Einstein–de Haas effect (see, e.g., Ref. [31]) or with x-ray magnetic circular dichroism (XMCD) [32–34]. The classic picture of the orbital moment is based on a superposition of atomiclike swirling charge currents [35]. For extended systems this picture is incomplete, as explained by the modern theory of orbital magnetization [36–41], with important extensions and clarifications developed more recently [42–44]. In Ref. [38] a separation of the orbital moment into local circulation and itinerant circulation was discussed. However, the interpretation of the latter contribution to the orbital moment remains subtle in bulk magnets. It is then insightful to bring the physics from reciprocal to real space by considering magnetic impurities on a nonmagnetic surface with strong SOC and the orbital magnetism they induce on the surrounding itinerant electrons.

In this paper, we formulate the orbital magnetic moment in real space in terms of the ground-state charge current density, partitioned into atomic and interatomic contributions. While the former corresponds to the often-studied atomiclike orbital angular momentum, the latter is unknown for magnetic nanostructures. Using first principles, we systematically study transition-metal single adatoms deposited on the Pt(111) surface. We find that the interatomic orbital moment is as large as the atomic one and, surprisingly, extends much farther into the substrate. This defines an interatomic orbital magnetization cloud three times larger than the previously found spin-polarization cloud hosted by the Pt atoms in the vicinity of magnetic atoms [7,8,45]. The moments induced in the substrate can be rationalized as different types of response of the surface to the presence of the magnetic adatom. In this way, we also prove that the separation into atomic and interatomic contributions is meaningful and that they have distinct physical origins. The interatomic contribution to the orbital moment is thus shown to be as important as the atomic one, which may have consequences for fundamental studies and possible technological applications.

II. METHODS

In classical electrodynamics, the net orbital moment $\mathbf{m}_\mathrm{o}$ arises from the charge current density $\mathbf{j}(\mathbf{r})$ [46],

$$\mathbf{m}_\mathrm{o} = \frac{1}{2}\int d\mathbf{r}\; \mathbf{r} \times \mathbf{j}(\mathbf{r}). \tag{1}$$

---

[*] s.brinker@fz-juelich.de
[†] m.dos.santos.dias@fz-juelich.de
[‡] s.lounis@fz-juelich.de

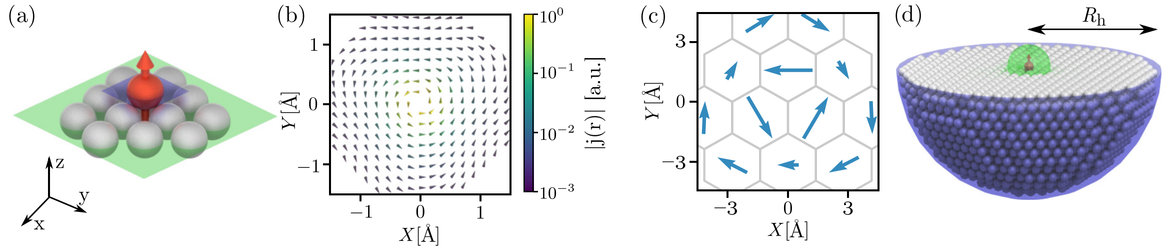

FIG. 1. Paramagnetic charge current created by an Fe adatom on the Pt(111) surface. (a) Atomic structure. The red sphere represents the adatom, and the gray ones show the Pt surface atoms. The magnetic moment of the adatom is sketched as a red arrow. The adatom is in the fcc-stacking position with the vertical distance to the surface reduced to 75% of the bulk interlayer distance. The cut planes for (b) and (c) are marked in purple and green, respectively. (b) Current within the Fe adatom. The color scale is logarithmic in atomic units. (c) Net charge currents $\mathbf{j}_i^{\mathrm{net}}$ in the surface layer of Pt(111). These yield the interatomic contribution to the orbital moment [see Eq. (5)]. (d) Giant cluster consisting of a small central cluster (green sphere) with a radius of 2.8 Å, and a large outer one (blue hemisphere) with a radius of $R_{\mathrm{h}} = 27.2$ Å, comprising 2685 Pt atoms.

This formula holds as long as $\mathbf{j}(\mathbf{r})$ decays quickly enough towards the boundaries of some enclosing volume. Microscopically, we can employ the quantum-mechanical ground-state current density, which has three contributions: paramagnetic, diamagnetic, and spin orbit [47]. The paramagnetic contribution is given by

$$\mathbf{j}(\mathbf{r}) = -i\,\mu_{\mathrm{B}}\{\Psi^{\dagger}(\mathbf{r})[\nabla\Psi(\mathbf{r})] - [\nabla\Psi^{\dagger}(\mathbf{r})]\,\Psi(\mathbf{r})\}, \quad (2)$$

where μ_{B} is the Bohr magneton and $\Psi(\mathbf{r})$ is the ground-state wave function (written for a single electronic coordinate for brevity), which can be written in a Green's function formalism as

$$\mathbf{j}(\mathbf{r}) = -i\,\mu_{\mathrm{B}} \lim_{\mathbf{r}'\to\mathbf{r}} (\nabla - \nabla')\mathrm{Tr}\,\rho(\mathbf{r},\mathbf{r}'), \quad (3)$$

where

$$\rho(\mathbf{r},\mathbf{r}') = \frac{1}{2\pi i}\int dE\, f(E)[G^{\dagger}(\mathbf{r}',\mathbf{r};E) - G(\mathbf{r},\mathbf{r}';E)] \quad (4)$$

is the density matrix (a 2 × 2 matrix in spin space, Tr is its trace), $f(E)$ is the Fermi-Dirac distribution function, and $G(\mathbf{r},\mathbf{r}';E)$ is the retarded single-particle Green's function. The diamagnetic current is absent (no external magnetic fields), and the relativistic correction to the current is found to be small [48], so it is also neglected. However, SOC itself is very important, as it lifts the orbital degeneracy of the surface (needed for a finite ground-state current) via the lifted spin degeneracy due to the presence of the magnetic adatom.

The ground-state paramagnetic current is thus the key to quantify the orbital magnetism induced by the adatom on the surface. The interpretation is facilitated by partitioning the geometry illustrated in Fig. 1(a) into regions centered around each atom, located at $\mathbf{R}_i$ and with volume $\mathcal{V}_i$. The orbital moment can then also be split,

$$\mathbf{m}_{\mathrm{o}} = \sum_i \frac{1}{2}\left(\mathbf{R}_i \times \mathbf{j}_i^{\mathrm{net}} + \int_{\mathcal{V}_i} d\mathbf{r}\;(\mathbf{r}-\mathbf{R}_i)\times\mathbf{j}(\mathbf{r})\right)$$
$$= \sum_i \left(\mathbf{m}_{\mathrm{o},i}^{\mathrm{ia}} + \mathbf{m}_{\mathrm{o},i}^{\mathrm{a}}\right) = \mathbf{m}_{\mathrm{o}}^{\mathrm{ia}} + \mathbf{m}_{\mathrm{o}}^{\mathrm{a}}. \quad (5)$$

Equation (5) is independent of the choice of origin (see Appendix A). The atomic contribution $\mathbf{m}_{\mathrm{o},i}^{\mathrm{a}}$ captures the swirling of the current around the ith atom [see Fig. 1(b)], which maps the atomic orbital angular momentum. The interatomic contribution $\mathbf{m}_{\mathrm{o},i}^{\mathrm{ia}}$ is due to the net currents $\mathbf{j}_i^{\mathrm{net}} = \int_{\mathcal{V}_i} d\mathbf{r}\,\mathbf{j}(\mathbf{r})$ that flow through the atoms [Fig. 1(c)]. With Eq. (5) we gain access to the spatial dependence of the interatomic contribution through $\mathbf{m}_{\mathrm{o},i}^{\mathrm{ia}}$.

To quantify the ground-state current in a realistic system, we first obtained a realistic geometry for the adatom on the surface with QUANTUM ESPRESSO supercell calculations [49], as explained in Appendix B. Then we employed a different calculation method based on a real-space embedding technique, which is possible with the Korringa-Kohn-Rostoker Green's function method [50–52]. In this way we avoid possible spurious effects due to the periodicity implied by supercell calculations and are able to reach much larger system sizes. The following steps were followed: First, the electronic structure of the pristine Pt(111) surface is obtained using a thick slab with open boundary conditions in the stacking direction. Then clusters of different sizes are self-consistently embedded in the pristine surface, taking into account the relaxation of the adatom towards the surface [see Fig. 1(d) for an example]. For this we utilize the Dyson equation

$$G(\mathbf{r},\mathbf{r}';E) = G_0(\mathbf{r},\mathbf{r}';E) + \int d\mathbf{r}_1\; G_0(\mathbf{r},\mathbf{r}_1;E)\Delta V(\mathbf{r}_1)G(\mathbf{r}_1,\mathbf{r}';E), \quad (6)$$

where $G(\mathbf{r},\mathbf{r}';E)$ is the Green's function of the surface including the magnetic adatoms, $G_0(\mathbf{r},\mathbf{r}';E)$ is the Green's function of the unperturbed surface, and $\Delta V(\mathbf{r})$ is the potential perturbation arising from the presence of the adatoms. Equation (6) can be reexpressed by replacing the potential perturbation by the respective scattering matrix $\Delta T(\mathbf{r},\mathbf{r}';E)$, yielding

$$G(\mathbf{r},\mathbf{r}';E) = G_0(\mathbf{r},\mathbf{r}';E) + \int d\mathbf{r}_1 \int d\mathbf{r}_2\; G_0(\mathbf{r},\mathbf{r}_1;E) \times \Delta T(\mathbf{r}_1,\mathbf{r}_2;E)G_0(\mathbf{r}_2,\mathbf{r}';E). \quad (7)$$

The induced currents and the associated orbital moments arise from the presence of the magnetic adatoms and so are described by the second part of Eq. (7). This term has the structure of a generalized response function of the surface, $G_0G_0 \sim \chi$, to the perturbation due to the adatoms ΔT. All quantities can then be systematically converged with respect to the cluster size. Further computational details can be found in Appendix B.

III. RESULTS

We first consider the generic features of the paramagnetic charge current, taking an Fe adatom on the Pt(111) surface as an example. The atomic structure is depicted in Fig. 1(a). Figure 1(b) illustrates the current distribution within the adatom. The current is localized near the nuclear position and swirls mostly in the xy plane, generating an atomic orbital moment parallel to the spin moment of the adatom. The adatom also induces a paramagnetic current in the surface. Part of it swirls around each Pt atom (not shown) and forms the atomic orbital moments $\mathbf{m}^{\mathrm{a}}_{\mathrm{o},i}$. The remainder leads to a net current through each Pt atom [Fig. 1(c)], resulting in the interatomic contributions $\mathbf{m}^{\mathrm{ia}}_{\mathrm{o},i}$. The direction of the swirl of the net currents is seen to alternate with distance, similar to the well-known Friedel oscillations of the charge and spin moment [1,8,53], so $\mathbf{m}^{\mathrm{ia}}_{\mathrm{o},i}$ also changes orientation with increasing distance to the adatom. The oscillations are due to the product of the unperturbed Green's functions G_0 in Eq. (7). These should then decay with a specific power law depending on the dimensionality of the host material, and a spatial anisotropy of the induced currents can arise depending on the shape of the constant-energy surfaces characterizing its electronic structure. Motivated by our *ab initio* results, we addressed recently [54] the case of magnetic impurities in a two-dimensional Rashba electron gas using a phenomenological model and showed that the decay of the paramagnetic current in the asymptotic limit should go as $1/r$ with oscillation wavelengths defined by the Rashba parameter, i.e., the spin-orbit coupling strength, and the Fermi-energy wavelength.

Next, we investigate the range of the induced magnetic moments, considering various adatoms. Fixing the spin moment of the adatom to be normal to the surface, $C_{3\mathrm{v}}$ symmetry ensures that the net induced moments are also collinear with it. Figure 2(a) plots the net spin moments m_{s} and the net atomic orbital moments $m^{\mathrm{a}}_{\mathrm{o}}$ against the size of the cluster, showing that they are well converged beyond a hemispherical radius of $R_{\mathrm{h}} \sim 7.5$ Å (55 Pt atoms). Surprisingly, the net interatomic orbital moment $m^{\mathrm{ia}}_{\mathrm{o}}$ has a much longer range than the other two [see Fig. 2(b)], going beyond the largest computationally feasible cluster (vertical dashed line). We tested a physical assumption to overcome the computational limitations: Is the response of a far-away Pt atom to the presence of the magnetic adatom independent of how its nearby Pt atoms respond? Working with a smaller cluster augmented by a far-away Pt atom and performing calculations for all possible positions of this extra atom, we obtain the response equivalent to that of a giant cluster with 2685 atoms, sketched in Fig. 1(d). We found that the interatomic orbital moments do follow the previous assumption (see Appendix D), validating the results shown in Fig. 2(b) beyond the vertical dashed line. $m^{\mathrm{ia}}_{\mathrm{o}}$ is converged only beyond $R_{\mathrm{h}} \sim 21$ Å, showing that it extends about three times as far as the other two contributions to the net induced magnetic moment.

The giant cluster approach can also be used to study the spatial distribution of the interatomic orbital moments. These

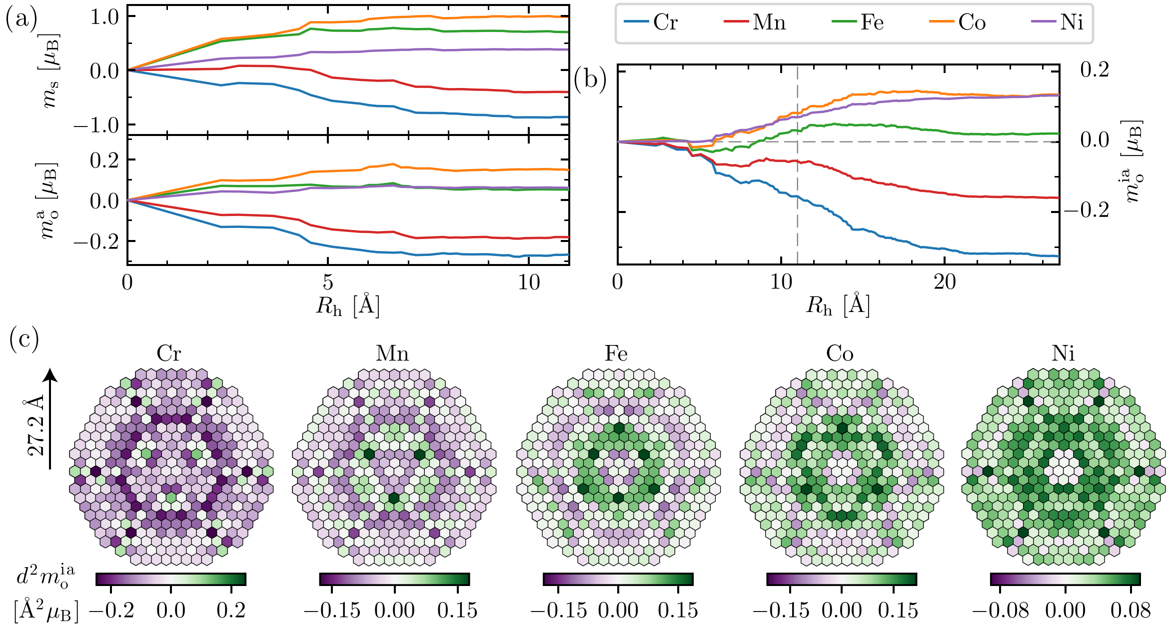

FIG. 2. Net induced magnetic moments on the Pt(111) surface due to several adatoms as a function of the hemispherical cluster radius R_{h}. (a) Net spin and atomic orbital moments, m_{s} and $m^{\mathrm{a}}_{\mathrm{o}}$. (b) Net interatomic orbital moments $m^{\mathrm{ia}}_{\mathrm{o}}$. The vertical dashed line at 11 Å marks the largest computationally feasible cluster (169 Pt atoms). The method described in the main text was utilized to obtain an effective hemispherical cluster with $R_{\mathrm{h}} = 27.2$ Å (2685 Pt atoms). Both methods lead to the same results for $m^{\mathrm{ia}}_{\mathrm{o}}$ (see Appendix D). (c) Spatial distribution of the interatomic orbital moments on the Pt surface layer, induced by various adatoms. The maps show the component of $\mathbf{m}^{\mathrm{ia}}_{\mathrm{o},i}$ normal to the surface. The values are scaled by the square of the distance d between a Pt atom and the adatom, showing that they decay faster than $1/d^2$.

TABLE I. Magnetic moments (in units of μ_{B}) generated by different adatoms on Pt(111). $m_{\mathrm{s}}^{\mathrm{ad}}$ and $m_{\mathrm{o}}^{\mathrm{ad}}$ are the spin and orbital moments of each adatom, and $P_{\mathrm{s}}^{\mathrm{ad}}$ is the relative spin polarization at the Fermi energy of each adatom. m_{s}, $m_{\mathrm{o}}^{\mathrm{a}}$, and $m_{\mathrm{o}}^{\mathrm{ia}}$ are the spin, atomic orbital, and interatomic orbital moments of Pt, induced by each adatom.

	Cr	Mn	Fe	Co	Ni
$m_{\mathrm{s}}^{\mathrm{ad}}$	2.83	3.90	3.46	2.26	0.59
$m_{\mathrm{o}}^{\mathrm{ad}}$	0.05	0.07	0.13	0.24	0.05
$P_{\mathrm{s}}^{\mathrm{ad}}$	−0.77	−0.51	0.58	0.83	0.32
m_{s}	−0.87	−0.41	0.70	0.98	0.38
$m_{\mathrm{o}}^{\mathrm{a}}$	−0.27	−0.18	0.05	0.15	0.06
$m_{\mathrm{o}}^{\mathrm{ia}}$	−0.32	−0.16	0.02	0.14	0.13
$\frac{m_{\mathrm{o}}^{\mathrm{ia}}}{m_{\mathrm{o}}^{\mathrm{ad}}+m_{\mathrm{o}}^{\mathrm{a}}}$	145%	145%	11%	35%	118%

are mapped in Fig. 2(c) for the Pt surface atoms, showing Friedel-like oscillations with a fast decay with the distance to a magnetic adatom. The nonmonotonic dependence of $m_{\mathrm{o}}^{\mathrm{ia}}$ on the cluster radius [see Fig. 2(b)] originates from these oscillations. They are most pronounced for the Fe adatom: The alternating signs of the Pt contributions with increasing distance to the adatom almost cancel each other out when added together. Surveying the maps for the other adatoms, we see that Ni (Cr) generates mostly positive (negative) contributions to $m_{\mathrm{o}}^{\mathrm{ia}}$, while the oscillations are still present for Co and Mn, although the net contribution is clearly positive for Co and negative for Mn.

The spin and orbital magnetic moments are collected in Table I. The spin and orbital moments of the adatoms follow from the filling of their d orbitals. Although those two quantities are not our primary interest, we note that their values might be underestimated and could be improved by a more sophisticated description of the intra-atomic electronic correlations [22,55]. The net spin, atomic, and interatomic orbital moments induced in Pt are seen to increase when going from Cr to Ni, with an antiparallel alignment for Cr and Mn with respect to the spin moment of the adatom. The simple Rashba model provides a qualitative explanation for this trend: The induced orbital magnetization in the Rashba model $m_{\mathrm{o}}^{\mathrm{R}}$ is found to be proportional to the magnetic part of the impurity potential and can be roughly approximated by $m_{\mathrm{o}}^{\mathrm{R}} \propto \mathrm{Re}\int^{E_{\mathrm{F}}} dE\, \frac{\Delta t(E)}{\sqrt{E}}$ [54], where $\Delta t = t_{\uparrow} - t_{\downarrow}$ is the difference of the scattering matrices for majority and minority impurity spin channels. Changing the chemical and magnetic nature of the adatom modifies $\Delta t(E)$, in particular its sign (see Fig. 3 in Ref. [54]), leading to the observed trend in the induced orbital moments.

The atomic and interatomic orbital moments induced in Pt are of similar magnitude. Furthermore, the interatomic orbital moment is a substantial part of the net orbital moment for all adatoms and is even the largest contribution for Cr, Mn, and Ni.

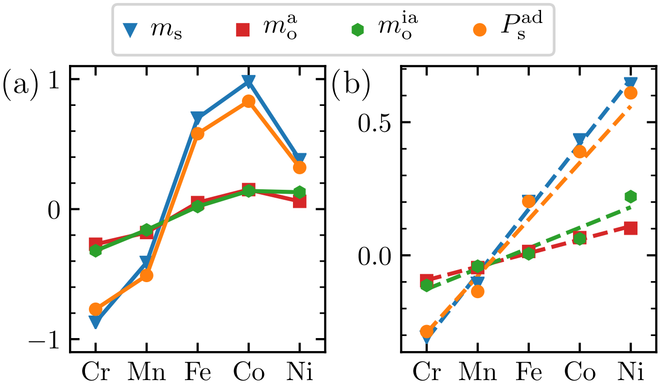

FIG. 3. Relations between the induced surface magnetic moments and the magnetic properties of the adatoms. (a) Spin (m_{s}), atomic ($m_{\mathrm{o}}^{\mathrm{a}}$), and interatomic ($m_{\mathrm{o}}^{\mathrm{ia}}$) orbital moments (in units of μ_{B}) and relative spin polarization at the Fermi energy $P_{\mathrm{s}}^{\mathrm{ad}}$ of each adatom. (b) Same as in (a), but with all quantities divided by the corresponding spin moment of each adatom $m_{\mathrm{s}}^{\mathrm{ad}}$ [see Eq. (8a)]. The dashed lines are linear fits to the data.

As argued in connection with Eq. (7), all the different induced magnetic moments can be seen as a response of the surface to the perturbation caused by the deposited adatoms, although the explicit connection is extremely complicated. Keeping the spirit of the argument, we will now show that the induced magnetic moments can be related to the local properties of the adatom in a simple way. Only two properties are required: the local spin moment $m_{\mathrm{s}}^{\mathrm{ad}}$ and the relative spin polarization at the Fermi energy of each adatom, $P_{\mathrm{s}}^{\mathrm{ad}} = \frac{\rho_{\downarrow}(E_{\mathrm{F}})-\rho_{\uparrow}(E_{\mathrm{F}})}{\rho_{\downarrow}(E_{\mathrm{F}})+\rho_{\uparrow}(E_{\mathrm{F}})}$, with $\rho_{\downarrow}(E_{\mathrm{F}})$ and $\rho_{\uparrow}(E_{\mathrm{F}})$ being the minority and majority spin-projected local densities of states of each adatom (see Appendix F), evaluated at the Fermi energy. The latter quantity is closely related to the induced spin moments, as made apparent in Fig. 3(a). We find that all the induced magnetic moments m^{ind} are linear in both $m_{\mathrm{s}}^{\mathrm{ad}}$ and $P_{\mathrm{s}}^{\mathrm{ad}}$,

$$m^{\mathrm{ind}} = \chi_m m_{\mathrm{s}}^{\mathrm{ad}} + \chi_P P_{\mathrm{s}}^{\mathrm{ad}} \tag{8a}$$

or

$$\frac{m^{\mathrm{ind}}}{m_{\mathrm{s}}^{\mathrm{ad}}} = \chi_m + \chi_P \frac{P_{\mathrm{s}}^{\mathrm{ad}}}{m_{\mathrm{s}}^{\mathrm{ad}}}, \tag{8b}$$

as shown in Fig. 3(b) with the fitted values of χ_m and χ_P given in Table II. The surface responds not only to the overall strength of the magnetic perturbation caused by each adatom $m_{\mathrm{s}}^{\mathrm{ad}}$ but also to the spin asymmetry at the Fermi energy $P_{\mathrm{s}}^{\mathrm{ad}}$. We interpret the former as the Fermi sea and the latter as the Fermi-surface part of an effective magnetic susceptibility of the surface.

Both $m_{\mathrm{o}}^{\mathrm{a}}$ and $m_{\mathrm{o}}^{\mathrm{ia}}$ arise from the combination of the strong SOC of Pt with the breaking of spin symmetry due to a magnetic adatom. Pt is well known to have a large Stoner enhancement of its spin susceptibility, which should be important not just for m_{s} but also for $m_{\mathrm{o}}^{\mathrm{a}}$ and $m_{\mathrm{o}}^{\mathrm{ia}}$, through its strong SOC. However, we verified that for $m_{\mathrm{o}}^{\mathrm{ia}}$ the response of a far-away Pt

TABLE II. Values of χ_m and χ_P as obtained from the fits in Fig. 3.

	χ_m	χ_P (units of μ_{B})
Spin moment	0.010	1.04
Atomic orbital moment	−0.026	0.21
Interatomic orbital moment	−0.024	0.32

atom is independent of how its nearby Pt atoms respond, while this is false for m_o^a and m_s (see Appendix D). This proves that m_o^ia represents a spin-orbital response of the surface which is distinct from the one leading to m_o^a, which could be suspected from their very different spatial ranges. A simple explanation is to imagine that each Pt atom responds to the magnetic adatom partly by generating a swirling current centered on it. This contributes locally to m_o^a but averages out for the local net current by superposing the contributions generated by the surrounding Pt atoms, leaving m_o^ia unaffected.

IV. CONCLUSIONS

We presented a theory of the interatomic orbital magnetism caused by magnetic nanostructures on a nonmagnetic surface, rooted in knowledge of the induced paramagnetic ground-state current density. Our detailed study of the magnetism of the Pt(111) surface induced by $3d$ adatoms uncovered several interesting properties of the interatomic orbital moment: It is long ranged, displays Friedel-like oscillations, and arises in a different way than the atomic orbital moment. The interatomic contribution to the orbital moment is as important as the atomic one and cannot be neglected. This is in stark contrast to the case of the elemental bulk ferromagnets, where the interatomic contribution was found to be small [39,41,56].

It remains to be explored whether XMCD measurements employing the sum-rule analysis can detect the full orbital moment of Pt or just part of it, as was argued in a different context in Ref. [38]. Detecting the magnetic stray field produced by the induced magnetic moments may be a viable alternative, exploiting the sensitivity of electron spin resonance via nitrogen-vacancy centers in diamond or proxy magnetic adatoms [57–59].

The type of surface and the size, shape, and dimension of the magnetic nanostructures will matter in defining the magnitude and the decay of the interatomic orbital moments. We found that on the Pt(111) surface the interatomic orbital moments extend three times farther than the atomic orbital and spin moments. This has the following important implication: Two nanostructures assumed to be decoupled based on the spatial range of the atomic orbital and spin moments might actually still be coupled via the interatomic orbital moments. This should be kept in mind when interpreting experimental findings. On the other hand, it might mediate new long-range interactions of the RKKY type through the orbital degrees of freedom, a point that requires further investigations and could be of potential interest for spin-orbitronics applications.

ACKNOWLEDGMENTS

We acknowledge very insightful discussions with J. Bouaziz. This work was supported by the European Research Council (ERC) under the European Union's Horizon 2020 research and innovation program (ERC consolidator Grant No. 681405 – DYNASORE). We gratefully acknowledge the computing time granted by the JARA-HPC Vergabegremium and VSR commission on the supercomputer JURECA at Forschungszentrum Jülich.

APPENDIX A: PROOF THAT THE TOTAL ORBITAL MOMENT IS INDEPENDENT OF THE CHOICE OF ORIGIN

In the following, we will show that the choice of origin does not influence the total orbital moment as defined in Eq. (5) in the main text or its decomposition into atomic and interatomic parts. Consider a fixed partition of space into cells surrounding each atom i, with volume $\mathcal{V}_i$. If we redefine the origin of each cell, $\mathbf{R}_i \to \mathbf{R}_i + \mathbf{T}$, we easily see that the atomic contributions to the orbital moment are unaffected by this shift. The interatomic part of the orbital moment transforms as follows:

$$\mathbf{m}_\mathrm{o}^\mathrm{ia} = \frac{1}{2}\sum_i (\mathbf{R}_i + \mathbf{T}) \times \mathbf{j}_i^\mathrm{net} \tag{A1}$$

$$= \frac{1}{2}\sum_i \mathbf{R}_i \times \mathbf{j}_i^\mathrm{net} + \frac{1}{2}\mathbf{T} \times \mathbf{j}^\mathrm{total}, \tag{A2}$$

where $\mathbf{j}^\mathrm{total} = \sum_i \mathbf{j}_i^\mathrm{net}$. Time-reversal-invariant surfaces do not host finite ground-state currents on their own, so the induced charge currents will be bound to swirl around the nanostructure. It follows that the total current vanishes, so it also vanishes for an arbitrary partition of space:

$$\mathbf{0} = \int d\mathbf{r}\, \mathbf{j}(\mathbf{r}) = \sum_i \int_{\mathcal{V}_i} d\mathbf{r}\, \mathbf{j}(\mathbf{r}) = \mathbf{j}^\mathrm{total}. \tag{A3}$$

This shows that the total interatomic orbital magnetic moment is independent of the choice of origin [see Eq. (A2)].

APPENDIX B: COMPUTATIONAL DETAILS FOR STANDARD CLUSTER CALCULATIONS

We performed density functional theory calculations with the Korringa-Kohn-Rostoker (KKR) Green's function method, with the potential in the atomic sphere approximation but with full charge density [50]. Exchange and correlation effects are treated in the local-spin-density approximation as parametrized by Vosko *et al.* [60], and SOC is added to the scalar-relativistic approximation [51]. The pristine surface is modeled by a slab of 40 Pt layers with the experimental lattice constant, 3.92 Å, with open boundary conditions in the stacking direction, and surrounded by two vacuum regions, each 9.06 Å thick. No relaxation of the surface layer is considered, as it was shown to be negligible [61]. We use 150 × 150 k points in the two-dimensional Brillouin zone, and the angular momentum expansions for the scattering problem are carried out up to $\ell_\mathrm{max} = 3$. In the next step, each adatom is placed in the fcc-stacking position on the Pt(111) surface, using an embedding method. Since the KKR method is not capable of structural relaxations, we used the plane-wave code QUANTUM ESPRESSO [49] to calculate the relaxation of an Fe atom towards the Pt surface. Using a 4 × 4 supercell with five layers of Pt and one k point, we found that the distance between the adatom and the surface layer is approximately 75% of the bulk interlayer distance. For the sake of comparison, we assume the same vertical distance for each adatom, as well as an out-of-plane spin moment, as depicted in Fig. 1(a). The embedding region consists of a spherical cluster with a radius of 2.8 Å around each magnetic adatom, augmented with a hemisphere of Pt atoms with a radius of 11.0 Å. This is a smaller version of the cluster sketched in Fig. 1(d). The current density is efficiently evaluated by utilizing a minimal *spdf* basis built out of regular scattering solutions evaluated at two or more energies by orthogonalizing their overlap matrix [52]. This is discussed in more detail in the following.

APPENDIX C: GROUND-STATE CURRENTS WITHIN THE KKR GREEN'S FUNCTION METHOD

The ground-state charge currents can be expressed in a Green's function formalism as shown in Eq. (3). Within our KKR implementation, we employ a set of basis functions designed for efficient calculations of response functions [52]. This basis is composed of normalized radial scattering solutions for each atomic cell i, with orbital (ℓ) and spin (s) angular momentum indices and basis index b, computed at several energies E_b within the range of the valence states,

$$\phi_{i\ell bs}(r) = \frac{R_{i\ell s}(r; E_b)}{\int dr\, r^2\, R_{i\ell s}(r; E_b)^2}. \tag{C1}$$

The basis construction is completed by orthogonalizing the overlap matrix and keeping the linear combinations with eigenvalues close to unity. The Green's function is expressed in the projection basis as ($\hat{\mathbf{r}} = \mathbf{r}/r$)

$$\begin{aligned} &G(\mathbf{r}+\mathbf{R}_i, \mathbf{r}'+\mathbf{R}_j; E) \\ &\quad = \sum_{\substack{Lb\\L'b'}} Y_L(\hat{\mathbf{r}})\phi_{i\ell b}(r)\, G_{iLb;jL'b'}(E)\, \phi_{j\ell'b'}(r')Y_{L'}(\hat{\mathbf{r}}'), \end{aligned} \tag{C2}$$

where $Y_L(\hat{\mathbf{r}})$ are real spherical harmonics with the combined index $L = (\ell, m)$ and $G_{iLb;jL'b'}(E)$ is the energy-dependent Green's function matrix element. Evaluating the energy integral of the Green's function matrix element, one obtains the density matrix in the projection basis,

$$\begin{aligned} &\rho(\mathbf{r}+\mathbf{R}_i, \mathbf{r}'+\mathbf{R}_j) \\ &\quad = \sum_{\substack{Lb\\L'b'}} Y_L(\hat{\mathbf{r}})\phi_{i\ell b}(r)\, \rho_{iLb;jL'b'}\, \phi_{j\ell'b'}(r')Y_{L'}(\hat{\mathbf{r}}'). \end{aligned} \tag{C3}$$

The action of the gradients in Eq. (3) on a basis consisting of spherical harmonics and a radial basis function can be simplified by utilizing the definition of the momentum operator, $\mathbf{p} = -i\nabla$, and the angular momentum operator, $\mathbf{L} = \mathbf{r}\times\mathbf{p}$,

$$\mathbf{r}\times\mathbf{L} = \mathbf{r}\times(\mathbf{r}\times\mathbf{p}) = r^2(\hat{\mathbf{r}}\cdot\mathbf{p})\hat{\mathbf{r}} - r^2\,\mathbf{p} \tag{C4}$$

$$\Longrightarrow \nabla = \hat{\mathbf{r}}\,\partial_r - i\,\frac{\hat{\mathbf{r}}\times\mathbf{L}}{r}, \tag{C5}$$

which yields

$$\nabla\phi_{i\ell b}(r)Y_L(\hat{\mathbf{r}}) = \hat{\mathbf{r}}(\partial_r\phi_{i\ell b}(r))Y_L(\hat{\mathbf{r}}) - i\,\frac{\phi_{i\ell b}(r)}{r}\hat{\mathbf{r}}\times[\mathbf{L}Y_L(\hat{\mathbf{r}})]. \tag{C6}$$

For computational reasons, we want to obtain the gradient in terms of new radial basis functions and spherical harmonics. Therefore, the remaining angular dependences in Eq. (C6) have to be rewritten in terms of spherical harmonics. Expressing the direction cosines in terms of spherical harmonics, $\hat{r}_\alpha = \sqrt{\frac{4\pi}{3}}Y_{\Lambda_\alpha}(\hat{\mathbf{r}})$, with $\Lambda_x = (1,1)$, $\Lambda_y = (1,-1)$, and $\Lambda_z = (1,0)$, and employing the Gaunt coefficients $C^{L_1}_{LL'}$, which convert products of two spherical harmonics (L, L') into a sum over single spherical harmonics (L_1), one finds for the vector components of the first term in Eq. (C6)

$$\hat{r}_\alpha\,(\partial_r\phi_{i\ell b}(r))\,Y_L(\hat{\mathbf{r}}) = \sqrt{\frac{4\pi}{3}}\,[\partial_r\phi_{i\ell b}(r)]\sum_{L_1} C^{L_1}_{\Lambda_\alpha L}\,Y_{L_1}(\hat{\mathbf{r}}). \tag{C7}$$

The action of the angular moment operator on spherical harmonics, which is needed for the second term in Eq. (C6), is given by the matrix elements of the angular momentum operator,

$$\hat{L}_\alpha Y_{\ell m}(\hat{\mathbf{r}}) = \sum_{m'} Y_{\ell m'}(\hat{\mathbf{r}})\,L^\alpha_{\ell,m'm}. \tag{C8}$$

For the second term in Eq. (C6) one then finds

$$\begin{aligned} &-i\,\frac{\phi_{i\ell b}(r)}{r}\,\{\hat{\mathbf{r}}\times[\mathbf{L}\,Y_L(\hat{\mathbf{r}})]\}_\alpha \\ &\quad = -i\,\frac{\phi_{i\ell b}(r)}{r}\sqrt{\frac{4\pi}{3}}\sum_{\beta\gamma}\epsilon_{\alpha\beta\gamma}\sum_{m'L_1} C^{L_1}_{\Lambda_\beta,\ell m'}\,L^\gamma_{\ell,m'm}\,Y_{L_1}(\hat{\mathbf{r}}). \end{aligned} \tag{C9}$$

Here $\epsilon_{\alpha\beta\gamma}$ is the Levi-Civita symbol. Combining this scheme with Eqs. (3) and (C3), the ground-state charge current can be straightforwardly calculated.

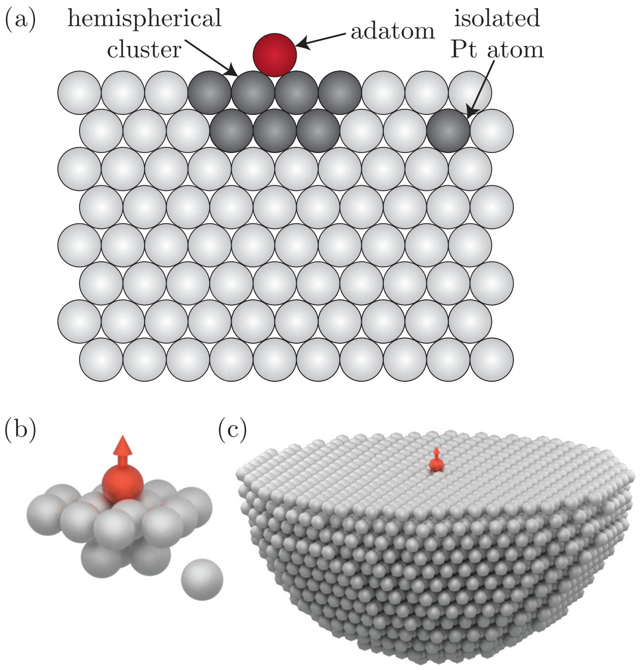

FIG. 4. Illustration of the cluster used for the giant hemispherical calculations. (a) The adatom (red sphere) is embedded on an arbitrary surface (light and dark gray spheres). The cluster used for each small calculation contains a hemisphere around the adatom (dark gray spheres) and one additional isolated host atom (dark gray sphere). (b) Three-dimensional visualization of the Pt(111) cluster used here. (c) Total giant hemispherical cluster containing 2685 Pt atoms, which is used for the calculation of the interatomic orbital moment.

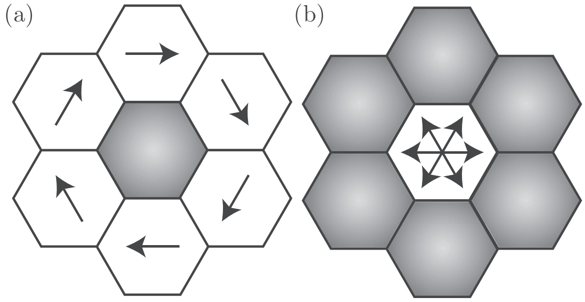

FIG. 5. Illustration of the induced net currents between Pt atoms. (a) A Pt atom (gray hexagon) induces net currents to its neighboring atoms, which are indicated by arrows and assumed to follow a clockwise swirling direction. (b) The net current induced from all the neighbors (gray hexagons) to the central Pt atom is shown as arrows.

APPENDIX D: COMPUTATIONAL DETAILS FOR GIANT CLUSTER CALCULATIONS

The interatomic orbital magnetic moments are obtained using a giant hemispherical cluster containing up to 2685 Pt atoms. In the following, we explain the construction of the giant cluster and the applicability of the method. The starting point is a self-consistent calculation for a small connected spherical cluster, which contains the adatom, 15 Pt atoms, and 9 vacuum sites, summing up to a total of 25 sites. One isolated Pt atom is then added to the previous cluster, as depicted in Figs. 4(a) and 4(b). Performing a single non-self-consistent iteration, we obtain the net ground-state charge current of the isolated Pt atom. Repeating this construction and utilizing the symmetry of the surface, we obtain the giant hemispherical cluster with 2685 Pt atoms shown in Fig. 4(c).

This approach does not account for the influence of the local environment of the isolated Pt atom on its net ground-state charge current, but it turns out that this is negligible. We verified this numerically but also found a qualitative explanation: Every Pt atom induces net currents into its neighboring atoms with a certain swirling direction, as sketched in Fig. 5(a). For a given atom, the sum of the contributions from all its neighbors will then tend to cancel, as indicated in Fig. 5(b), so that the contribution of the local environment of the atom to its net current will be negligible. We thus expect that the giant cluster approach should work well for the interatomic orbital moments since they depend only on the net charge currents.

This reasoning does not apply to the spin moment and the atomic orbital moment. Imagine a situation similar to the one depicted in Fig. 5 but for the spin moment: Now the

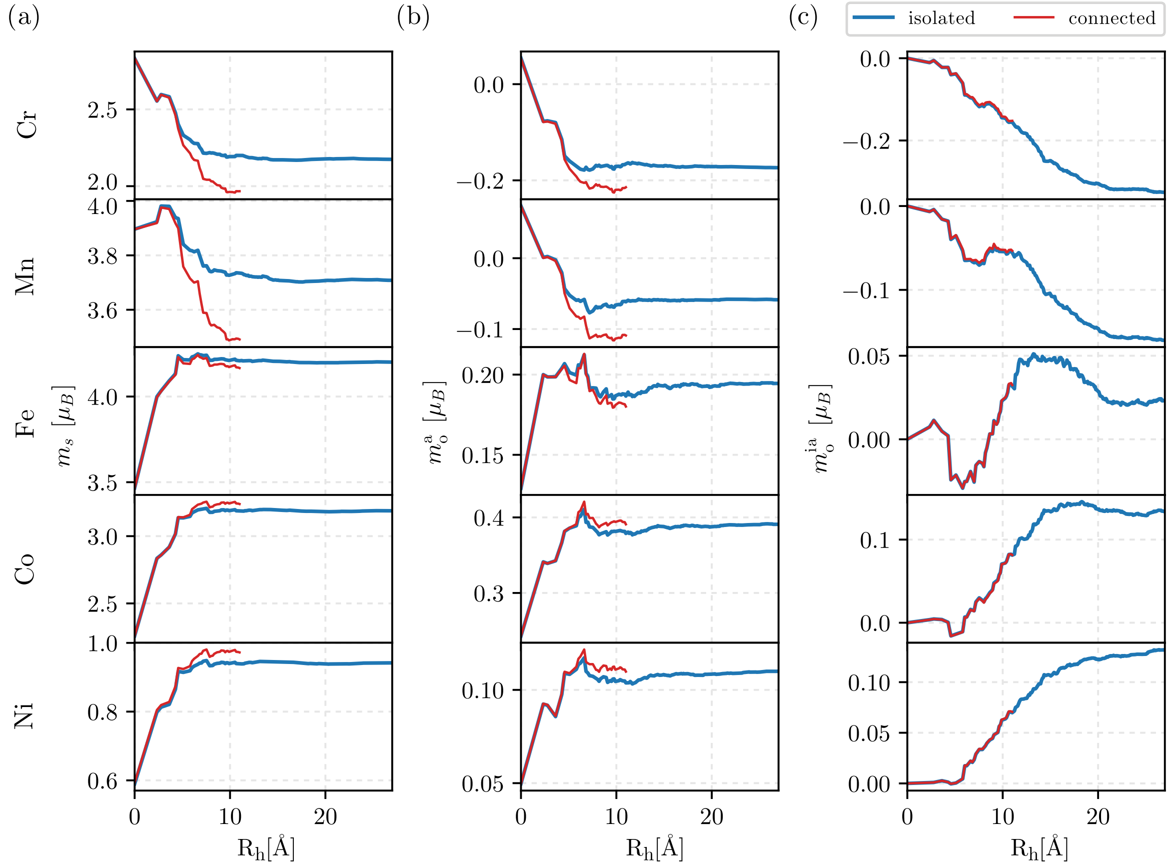

FIG. 6. Net magnetic moments as a function of the size of the cluster for the five adatoms, Cr, Mn, Fe, Co, and Ni, deposited on the Pt(111) surface: (a) spin moment, (b) atomic orbital moment, and (c) interatomic orbital moment. Each row pertains to the adatom indicated to the left of it. The results of the two different methods are shown: a connected hemispherical cluster (red line) and the method using isolated Pt atoms as described in the main text (blue curve). The deviations between the two methods for the spin moment and the atomic orbital moment are small but noticeable, while for the interatomic orbital moment both methods agree very well, with a small deviation of less than 2%.

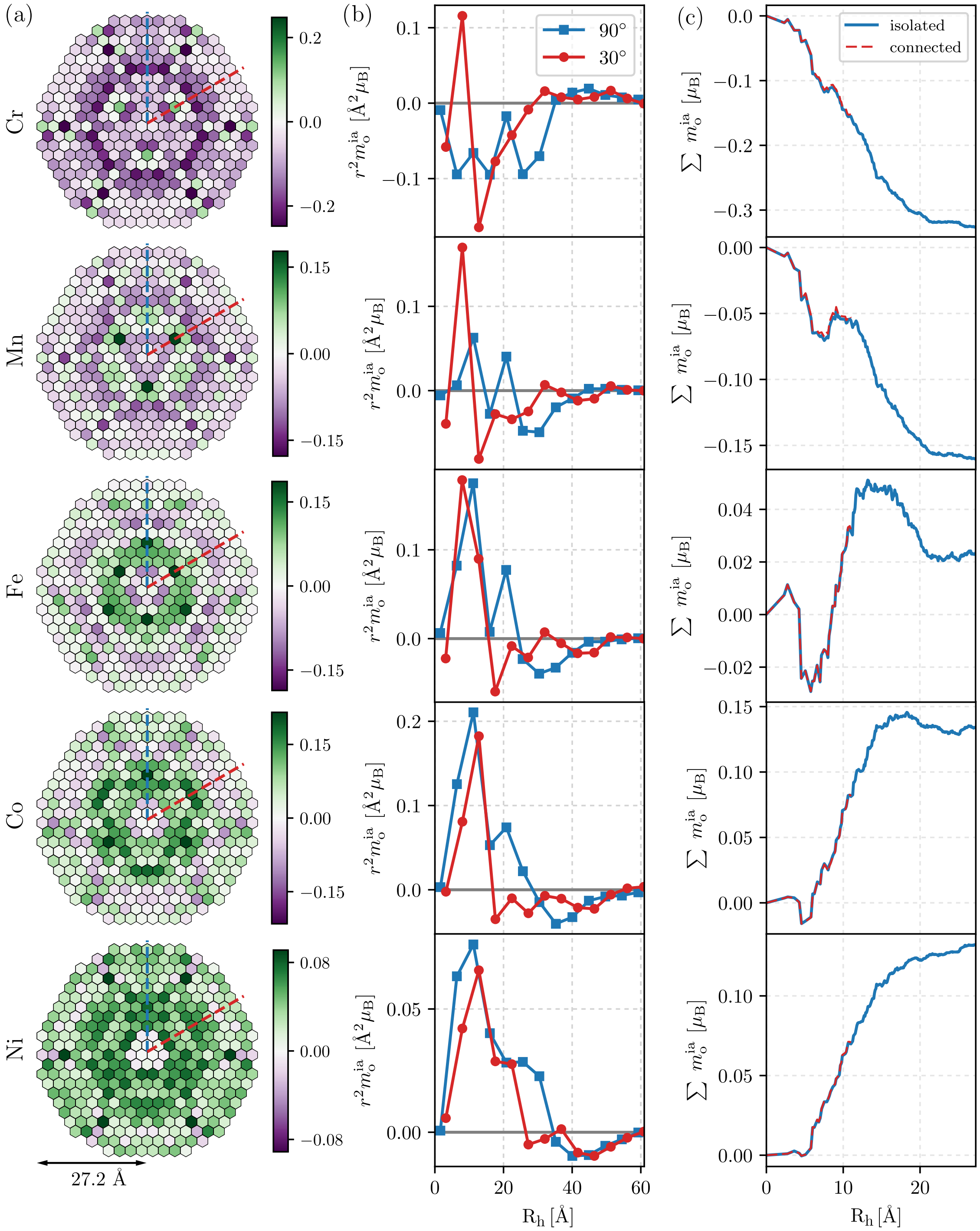

FIG. 7. Spatial distribution of the interatomic orbital moments for Cr, Mn, Fe, Co, and Ni deposited on the Pt(111) surface. Each row pertains to the adatom indicated to the left of it. (a) Interatomic orbital moment of the Pt atoms comprising the surface layer scaled by r^2. The red (30°) and blue (90°) dashed lines indicate two high-symmetry lines. (b) Directional dependence of the interatomic orbital moment in the surface layer of Pt(111) for the two high-symmetry directions scaled by r^2. The data points shown go beyond the clusters shown in (a). The oscillatory decay is faster than r^2. (c) Sum of the interatomic orbital moment over the full hemispherical cluster with a radius of 27.2 Å containing 2685 Pt atoms as a function of the distance to the adatom (blue solid line). The sum reaches a plateau at a distance of approximately 21.0 Å for all adatoms. The interatomic orbital moment from a connected cluster containing 169 Pt atoms (as discussed in the main text) is shown as a dashed red line. The results from both methods match, e.g., with a deviation of approximately 2% at a distance of 11.0 Å for the Fe adatom.

neighboring atoms of a given Pt atom will contribute to its induced spin moment. In contrast to the case of the net currents, there is no symmetry argument to suggest that the contributions from the neighbors should cancel out. The atomic orbital moment will also be affected, as it is connected to the local spin moment via spin-orbit coupling. Therefore, the spin moment and the atomic orbital moment might not be well described by our giant hemispherical cluster approach.

For a more quantitative picture, Fig. 6 shows the spin moment, the atomic orbital moment, and the interatomic orbital moment as a function of the hemispherical cluster size for the two different methods. The blue curves are the results of using isolated Pt atoms to scan a giant hemispherical cluster. The red curves correspond to a connected cluster with up to 169 Pt atoms, including all the effects of the local environment of each atom. For the spin moment [Fig. 6(a)] as well as the atomic orbital moment [Fig. 6(b)] one finds deviations of approximately 10% between the two methods for the Cr and Mn adatoms. For the other adatoms the deviation is below 5% but still noticeable. For the interatomic orbital moment [Fig. 6(c)] both methods agree very well, with deviations of less than 2%.

APPENDIX E: LONG-DISTANCE BEHAVIOR OF THE INTERATOMIC ORBITAL MOMENT

We next explore the distance dependence of the interatomic orbital moment for the five different adatoms deposited on the Pt(111) surface. Figure 7(a) shows the interatomic orbital moment in the Pt atoms comprising the surface layer. The red and blue dashed lines indicate two high-symmetry directions, which are used in Fig. 7(b) to show the long-distance behavior of the interatomic orbital moment. The decay does not depend on the chemical nature of the adatom, but it is an intrinsic property of the surface, as it is similar for all the different adatoms. Furthermore, the decay is faster than r^2, ensuring convergence of the net interatomic orbital moment. The giant hemispherical cluster calculations reach up to cluster sizes of 27.2 Å. From the line cuts we can estimate that enlarging the clusters would have minor effects, which lets us conclude that the values in Fig. 7(c) are converged.

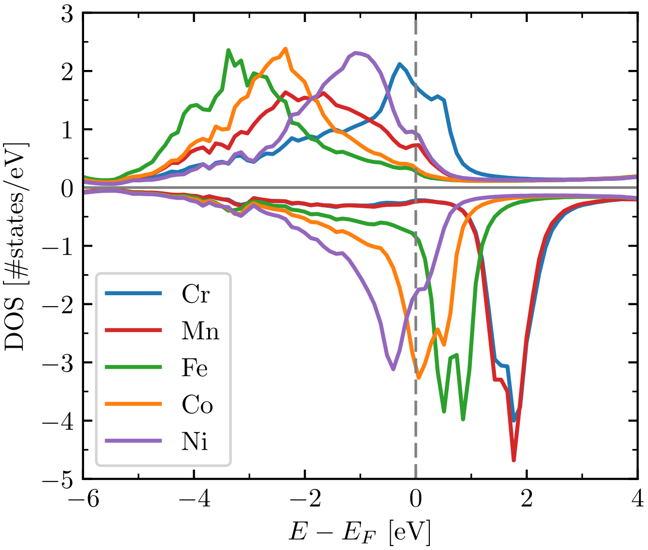

FIG. 8. Local density of states of the different adatoms deposited on the Pt(111) surface. Positive (negative) values correspond to the majority (minority) channel.

APPENDIX F: LOCAL DENSITY OF STATES OF THE ADATOMS

Figure 8 shows the local density of states of the five different adatoms deposited on the Pt(111) surface. The positive values show the majority spin channel, whereas the negative values indicate the minority spin channel. The spin polarization at the Fermi level as described in the main text can be obtained from the local density of states. From Fig. 8 we see that the majority spin channel is strongly hybridized with the surface electronic states, leading to a broad energy distribution of the *d* states of the adatoms, while the minority *d* states of the adatoms are less hybridized.

---

[1] J. Friedel, Metallic alloys, Nuovo Cimento **7**, 287 (1958).

[2] G. G. Low and T. M. Holden, Distribution of the ferromagnetic polarization induced by iron and cobalt atoms in palladium, Proc. Phys. Soc. London **89**, 119 (1966).

[3] G. J. Nieuwenhuys, Magnetic behavior of cobalt, iron and manganese dissolved in palladium, Adv. Phys. **24**, 515 (1975).

[4] A. Oswald, R. Zeller, and P. H. Dederichs, Giant Moments in Palladium, Phys. Rev. Lett. **56**, 1419 (1986).

[5] R. Zeller, Large-scale electronic-structure calculations for isolated transition-metal impurities in palladium, Modell. Simul. Mater. Sci. Eng. **1**, 553 (1993).

[6] T. Herrmannsdörfer, S. Rehmann, W. Wendler, and F. Pobell, Magnetic properties of highly diluted PdFe$_x$ and PtFe$_x$-alloys. Part I. Magnetization at Kelvin temperatures, J. Low Temp. Phys. **104**, 49 (1996).

[7] A. A. Khajetoorians, T. Schlenk, B. Schweflinghaus, M. dos Santos Dias, M. Steinbrecher, M. Bouhassoune, S. Lounis, J. Wiebe, and R. Wiesendanger, Spin Excitations of Individual Fe Atoms on Pt(111): Impact of the Site-Dependent Giant Substrate Polarization, Phys. Rev. Lett. **111**, 157204 (2013).

[8] M. Bouhassoune, M. dos Santos Dias, B. Zimmermann, P. H. Dederichs, and S. Lounis, RKKY-like contributions to the magnetic anisotropy energy: 3*d* adatoms on Pt(111) surface, Phys. Rev. B **94**, 125402 (2016).

[9] F. Meier, L. Zhou, J. Wiebe, and R. Wiesendanger, Revealing magnetic interactions from single-atom magnetization curves, Science **320**, 82 (2008).

[10] L. Zhou, J. Wiebe, S. Lounis, E. Vedmedenko, F. Meier, S. Blügel, P. H. Dederichs, and R. Wiesendanger, Strength and directionality of surface Ruderman–Kittel–Kasuya–Yosida interaction mapped on the atomic scale, Nat. Phys. **6**, 187 (2010).

[11] J. Klinovaja, P. Stano, A. Yazdani, and D. Loss, Topological Superconductivity and Majorana Fermions in RKKY Systems, Phys. Rev. Lett. **111**, 186805 (2013).

[12] S. Nadj-Perge, I. K. Drozdov, B. A. Bernevig, and A. Yazdani, Proposal for realizing Majorana fermions in chains of magnetic atoms on a superconductor, Phys. Rev. B **88**, 020407 (2013).

[13] F. Pientka, L. I. Glazman, and F. von Oppen, Topological superconducting phase in helical Shiba chains, Phys. Rev. B **88**, 155420 (2013).

[14] S. Nadj-Perge, I. K. Drozdov, J. Li, H. Chen, S. Jeon, J. Seo, A. H. MacDonald, B. A. Bernevig, and A. Yazdani, Observation of Majorana fermions in ferromagnetic atomic chains on a superconductor, Science **346**, 602 (2014).

[15] H. Prüser, P. E. Dargel, M. Bouhassoune, R. G. Ulbrich, T. Pruschke, S. Lounis, and M. Wenderoth, Interplay between the Kondo effect and the Ruderman-Kittel-Kasuya-Yosida interaction, Nat. Commun. **5**, 5417 (2014).

[16] N. Nagaosa, J. Sinova, S. Onoda, A. H. MacDonald, and N. P. Ong, Anomalous Hall effect, Rev. Mod. Phys. **82**, 1539 (2010).

[17] R. Yu, W. Zhang, H.-J. Zhang, S.-C. Zhang, X. Dai, and Z. Fang, Quantized anomalous Hall effect in magnetic topological insulators, Science **329**, 61 (2010).

[18] C.-Z. Chang, J. Zhang, X. Feng, J. Shen, Z. Zhang, M. Guo, K. Li, Y. Ou, P. Wei, L.-L. Wang, Z.-Q. Ji, Y. Feng, S. Ji, X. Chen, J. Jia, X. Dai, Z. Fang, S.-C. Zhang, K. He, Y. Wang, L. Lu, X.-C. Ma, and Q.-K. Xue, Experimental observation of the quantum anomalous Hall effect in a magnetic topological insulator, Science **340**, 167 (2013).

[19] A. Fert and P. M. Levy, Role of Anisotropic Exchange Interactions in Determining the Properties of Spin-Glasses, Phys. Rev. Lett. **44**, 1538 (1980).

[20] M. Menzel, Y. Mokrousov, R. Wieser, J. E. Bickel, E. Vedmedenko, S. Blügel, S. Heinze, K. von Bergmann, A. Kubetzka, and R. Wiesendanger, Information Transfer by Vector Spin Chirality in Finite Magnetic Chains, Phys. Rev. Lett. **108**, 197204 (2012).

[21] A. A. Khajetoorians, M. Steinbrecher, M. Ternes, M. Bouhassoune, M. dos Santos Dias, S. Lounis, J. Wiebe, and R. Wiesendanger, Tailoring the chiral magnetic interaction between two individual atoms, Nat. Commun. **7**, 10620 (2016).

[22] P. Gambardella, S. Rusponi, M. Veronese, S. S. Dhesi, C. Grazioli, A. Dallmeyer, I. Cabria, R. Zeller, P. H. Dederichs, K. Kern, C. Carbone, and H. Brune, Giant magnetic anisotropy of single cobalt atoms and nanoparticles, Science **300**, 1130 (2003).

[23] C. F. Hirjibehedin, C.-Y. Lin, A. F. Otte, M. Ternes, C. P. Lutz, B. A. Jones, and A. J. Heinrich, Large magnetic anisotropy of a single atomic spin embedded in a surface molecular network, Science **317**, 1199 (2007).

[24] F. Donati, A. Singha, S. Stepanow, C. Wäckerlin, J. Dreiser, P. Gambardella, S. Rusponi, and H. Brune, Magnetism of Ho and Er Atoms on Close-Packed Metal Surfaces, Phys. Rev. Lett. **113**, 237201 (2014).

[25] I. G. Rau, S. Baumann, S. Rusponi, F. Donati, S. Stepanow, L. Gragnaniello, J. Dreiser, C. Piamonteze, F. Nolting, S. Gangopadhyay, O. R. Albertini, R. M. Macfarlane, C. P. Lutz, B. A. Jones, P. Gambardella, A. J. Heinrich, and H. Brune, Reaching the magnetic anisotropy limit of a 3d metal atom, Science **344**, 988 (2014).

[26] R. Skomski, *Simple Models of Magnetism* (Oxford University Press, Oxford, 2008).

[27] R. Shindou and N. Nagaosa, Orbital Ferromagnetism and Anomalous Hall Effect in Antiferromagnets on the Distorted fcc Lattice, Phys. Rev. Lett. **87**, 116801 (2001).

[28] G. Tatara and N. Garcia, Quantum Toys for Quantum Computing: Persistent Currents Controlled by the Spin Josephson Effect, Phys. Rev. Lett. **91**, 076806 (2003).

[29] M. Hoffmann, J. Weischenberg, B. Dupé, F. Freimuth, P. Ferriani, Y. Mokrousov, and S. Heinze, Topological orbital magnetization and emergent Hall effect of an atomic-scale spin lattice at a surface, Phys. Rev. B **92**, 020401 (2015).

[30] M. dos Santos Dias, J. Bouaziz, M. Bouhassoune, S. Blügel, and S. Lounis, Chirality-driven orbital magnetic moments as a new probe for topological magnetic structures, Nat. Commun. **7**, 13613 (2016).

[31] A. J. P. Meyer and G. Asch, Experimental g′ and g values of Fe, Co, Ni, and their alloys, J. Appl. Phys. **32**, S330 (1961).

[32] B. T. Thole, P. Carra, F. Sette, and G. van der Laan, X-ray Circular Dichroism as a Probe of Orbital Magnetization, Phys. Rev. Lett. **68**, 1943 (1992).

[33] P. Carra, B. T. Thole, M. Altarelli, and X. Wang, X-ray Circular Dichroism and Local Magnetic Fields, Phys. Rev. Lett. **70**, 694 (1993).

[34] C. T. Chen, Y. U. Idzerda, H.-J. Lin, N. V. Smith, G. Meigs, E. Chaban, G. H. Ho, E. Pellegrin, and F. Sette, Experimental Confirmation of the X-ray Magnetic Circular Dichroism Sum Rules for Iron and Cobalt, Phys. Rev. Lett. **75**, 152 (1995).

[35] L. L. Hirst, The microscopic magnetization: concept and application, Rev. Mod. Phys. **69**, 607 (1997).

[36] D. Xiao, J. Shi, and Q. Niu, Berry Phase Correction to Electron Density of States in Solids, Phys. Rev. Lett. **95**, 137204 (2005).

[37] T. Thonhauser, D. Ceresoli, D. Vanderbilt, and R. Resta, Orbital Magnetization in Periodic Insulators, Phys. Rev. Lett. **95**, 137205 (2005).

[38] I. Souza and D. Vanderbilt, Dichroic f-sum rule and the orbital magnetization of crystals, Phys. Rev. B **77**, 054438 (2008).

[39] D. Ceresoli, U. Gerstmann, A. P. Seitsonen, and F. Mauri, First-principles theory of orbital magnetization, Phys. Rev. B **81**, 060409 (2010).

[40] T. Thonhauser, Theory of orbital magnetization in solids, Int. J. Mod. Phys. B **25**, 1429 (2011).

[41] J.-P. Hanke, F. Freimuth, A. K. Nandy, H. Zhang, S. Blügel, and Y. Mokrousov, Role of Berry phase theory for describing orbital magnetism: From magnetic heterostructures to topological orbital ferromagnets, Phys. Rev. B **94**, 121114 (2016).

[42] R. Bianco and R. Resta, Mapping topological order in coordinate space, Phys. Rev. B **84**, 241106 (2011).

[43] R. Bianco and R. Resta, Orbital Magnetization as a Local Property, Phys. Rev. Lett. **110**, 087202 (2013).

[44] A. Marrazzo and R. Resta, Irrelevance of the Boundary on the Magnetization of Metals, Phys. Rev. Lett. **116**, 137201 (2016).

[45] J. Hermenau, J. Ibañez-Azpiroz, C. Hübner, A. Sonntag, B. Baxevanis, K. T. Ton, M. Steinbrecher, A. A. Khajetoorians, M. dos Santos Dias, S. Blügel, R. Wiesendanger, S. Lounis, and J. Wiebe, A gateway towards non-collinear spin processing using three-atom magnets with strong substrate coupling, Nat. Commun. **8**, 642 (2017).

[46] J. D. Jackson, *Classical Electrodynamics*, 3rd ed. (Wiley, New York, 1999).

[47] S. Maekawa, *Spin Current*, Oxford Science Publications Vol. 17 (Oxford University Press, Oxford, 2012).

[48] S. Brinker, First-principles investigation of charge and spin currents in magnetic nanostructures, master's thesis, RWTH Aachen, 2016.

[49] P. Giannozzi, O. Andreussi, T. Brumme, O. Bunau, M. B. Nardelli, M. Calandra, R. Car, C. Cavazzoni, D. Ceresoli, M. Cococcioni, N. Colonna, I. Carnimeo, A. D. Corso, S. de Gironcoli, P. Delugas, R. A. DiStasio, Jr., A. Ferretti, A. Floris, G. Fratesi, G. Fugallo *et al.*, Advanced capabilities for materials modeling with Quantum Espresso, J. Phys.: Condens. Matter **29**, 465901 (2017).

[50] N. Papanikolaou, R. Zeller, and P. H. Dederichs, Conceptual improvements of the KKR method, J. Phys.: Condens. Matter **14**, 2799 (2002).

[51] D. S. G. Bauer, Development of a relativistic full-potential first-principles multiple scattering Green function method applied to complex magnetic textures of nano structures at surfaces, Ph.D. thesis, RWTH Aachen, 2014.

[52] M. dos Santos Dias, B. Schweflinghaus, S. Blügel, and S. Lounis, Relativistic dynamical spin excitations of magnetic adatoms, Phys. Rev. B **91**, 075405 (2015).

[53] S. Lounis, A. Bringer, and S. Blügel, Magnetic Adatom Induced Skyrmion-Like Spin Texture in Surface Electron Waves, Phys. Rev. Lett. **108**, 207202 (2012).

[54] J. Bouaziz, M. dos Santos Dias, F. Souza Mendes Guimarães, S. Blügel, and S. Lounis, Impurity-induced orbital magnetization in a Rashba electron gas, Phys. Rev. B (to be published) [arXiv:1806.02158].

[55] A. B. Shick and A. I. Lichtenstein, Orbital moment of a single Co atom on a Pt(111) surface—A view from correlated band theory, J. Phys.: Condens. Matter **20**, 015002 (2008).

[56] H. Ebert, M. Battocletti, and E. K. U. Gross, Current density functional theory of spontaneously magnetised solids, Europhys. Lett. **40**, 545 (1997).

[57] A. V. Balatsky, M. Nishijima, and Y. Manassen, Electron spin resonance-scanning tunneling microscopy, Adv. Phys. **61**, 117 (2012).

[58] L. Rondin, J.-P. Tetienne, T. Hingant, J.-F. Roch, P. Maletinsky, and V. Jacques, Magnetometry with nitrogen-vacancy defects in diamond, Rep. Prog. Phys. **77**, 056503 (2014).

[59] S. Baumann, W. Paul, T. Choi, C. P. Lutz, A. Ardavan, and A. J. Heinrich, Electron paramagnetic resonance of individual atoms on a surface, Science **350**, 417 (2015).

[60] S. H. Vosko, L. Wilk, and M. Nusair, Accurate spin-dependent electron liquid correlation energies for local spin density calculations: A critical analysis, Can. J. Phys. **58**, 1200 (1980).

[61] P. Błoński and J. Hafner, Density-functional theory of the magnetic anisotropy of nanostructures: An assessment of different approximations, J. Phys.: Condens. Matter **21**, 426001 (2009).